PHOTONICS Research

Versatile on-chip light coupling and (de)multiplexing from arbitrary polarizations to controlled waveguide modes using an integrated dielectric metasurface

YUAN MENG,[1,2,†] ZHOUTIAN LIU,[1,3,†] ZHENWEI XIE,[4] RIDE WANG,[5] TIANCHENG QI,[1,3] FUTAI HU,[1] HYUNSEOK KIM,[2,6] QIRONG XIAO,[1,3,*] XING FU,[1,3] QIANG WU,[5] SANG-HOON BAE,[2,6] MALI GONG,[1,3,7] AND XIAOCONG YUAN[4]

[1]State Key Laboratory of Precision Measurement Technology and Instruments, Department of Precision Instrument, Tsinghua University, Beijing 100084, China
[2]Research Laboratory of Electronics, Massachusetts Institute of Technology, Cambridge, Massachusetts 02139, USA
[3]Key Laboratory of Photonic Control Technology, Ministry of Education, Tsinghua University, Beijing 100084, China
[4]Nanophotonics Research Centre, Shenzhen Key Laboratory of Micro-Scale Optical Information Technology, Shenzhen University, Shenzhen 518060, China
[5]Key Laboratory of Weak-Light Nonlinear Photonics, Ministry of Education, TEDA Institute of Applied Physics and School of Physics, Nankai University, Tianjin 300457, China
[6]Department of Mechanical Engineering, Massachusetts Institute of Technology, Cambridge, Massachusetts 02139, USA
[7]e-mail: gongml@mail.tsinghua.edu.cn
*Corresponding author: xiaoqirong@mail.tsinghua.edu.cn

Received 27 November 2019; revised 12 January 2020; accepted 23 January 2020; posted 23 January 2020 (Doc. ID 384449); published 1 April 2020

Metasurfaces have found broad applicability in free-space optics, while its potential to tailor guided waves remains barely explored. By synergizing the Jones matrix model with generalized Snell's law under the phase-matching condition, we propose a universal design strategy for versatile on-chip mode-selective coupling with polarization sensitivity, multiple working wavelengths, and high efficiency concurrently. The coupling direction, operation frequency, and excited mode type can be designed at will for arbitrary incident polarizations, outperforming previous technology that only works for specific polarizations and lacks versatile mode controllability. Here, using silicon-nanoantenna-patterned silicon-nitride photonic waveguides, we numerically demonstrate a set of chip-scale optical couplers around 1.55 μm, including mode-selective directional couplers with high coupling efficiency over 57% and directivity about 23 dB. Polarization and wavelength demultiplexer scenarios are also proposed with 67% maximum efficiency and an extinction ratio of 20 dB. Moreover, a chip-integrated twisted light generator, coupling free-space linear polarization into an optical vortex carrying $1\hbar$ orbital angular momentum (OAM), is also reported to validate the mode-control flexibility. This comprehensive method may motivate compact wavelength/polarization (de)multiplexers, multifunctional mode converters, on-chip OAM generators for photonic integrated circuits, and high-speed optical telecommunications.

https://doi.org/10.1364/PRJ.384449

1. INTRODUCTION

Recent advancements in photonic integrated circuits have ushered emerging applications in optical information processing [1,2], lab-on-a-chip sensing systems [3,4], integrated quantum photonics [5,6], and high-speed chip-scale optical interconnects with low power consumption [7,8]. As an indispensable component that wires external light sources into photonic chips, optical couplers are of crucial significance [9]. While the coupling efficiency is an important figure of merit in these systems, it is also highly desired to achieve directional coupling with flexible wavelength, polarization, and even mode selectivity for both classic and quantum scenarios [10,11]. For instance, multiplexers/demultiplexers in optical communication systems employing the wavelength-division multiplexing technique [12]. However, conventional optical components to realize the abovementioned functionalities are generally bulky, which severely hinders further integration and practicality [13–15].

As an array of elaborately engineered optical scatterers with subwavelength spacing and spatially varying geometric parameters [16,17], the metasurface has found fertile soil in numerous applications, such as planar optics [18], high-efficiency holograms [19], ultrathin cloak [20], color display [21–23], and emerging fields in nonlinear [24,25] and topological photonics [26]. In contrast, their excellent potentiality to manipulate guided electromagnetic waves is not fully exploited. By incorporating the metasurface with the most fundamental building block of optical waveguides, the aforementioned coupling issues in integrated photonics can be addressed [17]. The flexibility and configurability harvested from optical antenna arrays can enable novel waveguide couplers with a compact footprint and versatile functionalities [27].

Previous similar research started from the directional excitation of surface plasmon polaritons using the gradient-index metasurface [28,29]. In terms of guided waves, plasmonic antennas are deployed to realize directional waveguide coupling [17,30–35]. However, metal antennas suffer from intrinsically high Ohmic loss [27]. The proposed dipole interference model [31–33] can design double-antennas or small arrays, but encounters challenges in upscaling to realize sophisticated optical systems. Recently, the gradient metasurface was applied to realize directional coupling [17,36,37], using either propagation [33,34] or geometric phase metasurface [36,37]. However, for designs adopting propagation phase concept [38–40], one given array only works for one specific linear polarization [31–33]. In contrast, the geometric phase (or Pancharatnam–Berry phase) metasurface [41,42] is solely applicable for circular polarizations, where an unconfigurable conjugate phase profile is always accompanied for the other orthogonal circular polarization [33,34] and the excited waveguide mode type cannot be controlled at will. As most of the devices in silicon- and silicon-nitride photonics have polarization-sensitive performance [1,7], mode-controllable waveguiding is highly favorable. Nevertheless, a universal design model working for arbitrary incident polarizations and that can simultaneously achieve coupled-mode selectivity with multiple working wavelengths is still elusive.

Here we propose a comprehensive design method with fabrication robustness to address versatile on-chip coupling and mode conversion applications in photonic integrated circuits, by synergizing the Jones matrix model [38–41,43] with generalized Snell's law [18] under the phase-matching condition for dielectric nanoantennas. Accommodating both propagation and geometric phase metasurface, the coupling direction, operation wavelength, and excited mode type can be designed at will for arbitrary incident polarizations. We apply silicon (Si) nanoantennas-patterned silicon-nitride (SiN) optical waveguides around the telecommunication wavelength of 1.55 μm to mitigate loss [44]. The high-index contrast dielectric here is also favorable for efficient antenna excitation. Representative design scenarios are numerically demonstrated, such as mode-selective chip-integrated directional couplers (with high coupling efficiency over 57% and directivity about 23 dB), versatile polarization demultiplexers and wavelength routers (with maximum coupling efficiency around 67% and extinction ratio of 20 dB for arbitrary incident polarization), and broadband chip-scale twisted light generators [that directly couple incident linear polarizations into the optical vortex carrying configurable orbital angular momentum (OAM) topological charge $\ell = \pm 1$]. Compared with previous similar works without applying the phase-matching condition [32,33,41], an at least 10-fold enhancement in coupling efficiency is numerically validated here. Moreover, in this work not only the fundamental TE_{00} and TM_{00} modes [41] but also the selective-excitation of desired high-order waveguide modes (for example, TE_{01}, TE_{10}, TM_{11}, and TM_{20}) with high mode purity is systematically investigated. Our method can also outperform former literature (only applicable for circular polarizations) [36,37], where the excited waveguide mode type cannot be arbitrarily controlled [36] or the directionality and high efficiency are not simultaneously achieved at the same operation wavelength [37]. The influence of the coupling condition and device fabrication error is also discussed. This universal design method may open new possibilities for further chip-scale photonic applications, such as integrated polarization (de)multiplexers, light routers, multifunctional mode converters, and on-chip configurable vortex beam generators.

2. FUNDAMENTALS AND DESIGN PRINCIPLES

Acting as form-birefringence elements [43], dielectric nanoantennas can impart a configurable, polarization- and wavelength-dependent phase to incident electromagnetic wave and simultaneously alter the polarization state of transmitted light [40,45,46]. A periodic antenna array (metasurface) functioning like a birefringent wave plate can be modeled by a Jones matrix $\mathbf{J}$ [38–41], which is unitary and symmetric (see Appendix A for details) and thus can be decomposed into eigenvalues (or eigenphases φ_x and φ_y) determined by antenna geometry and eigenvectors depending on the antenna's rotation angle θ. Therefore, for any arbitrary unit incident $|\lambda\rangle$ and transmitted $|\kappa\rangle$ polarization vectors, we can always find a Jones matrix $\mathbf{J}$ to enable the mapping $\mathbf{J}|\lambda\rangle = |\kappa\rangle$ guaranteed by the matrix theorem [40,41].

For high-index optical antennas like Si used here, the electromagnetic energy is mainly confined inside the antenna, while the impact from adjacent antennas is much weaker and negligible [40,41,47]. Consequently, we can divide an array into pixels (m, n) modeled by different Jones matrices $\mathbf{J}(m, n)$. This model unifies propagation and geometric phase metasurfaces [40,41]. Both the geometric parameters and rotation angle of the antenna pixels are engineered to achieve complete control over phase and polarization of the transmitted light for arbitrary incident polarizations [see Fig. 1(a)].

Considering the generalized Snell's law of transmission [48], for an optical waveguide patterned with a gradient metasurface, one specific waveguide mode can be selectively excited if the phase-matching condition is satisfied [17]:

$$(n_t \sin\theta_t - n_i \sin\theta_i)k_0 = n_{\text{eff}} k_0 = \frac{\Delta\varphi}{d} \cdot \text{sign}\left(\frac{\Delta\varphi}{d}\right), \quad \textbf{(1)}$$

where n_t and n_i are the refractive indices of transmitted and incident medium [48]. We have the effective mode index $n_t \sin\theta_t \equiv n_{\text{eff}}$ for guided waves [12] and incident angle $\theta_i = 0°$ under normal incidence [36,37] [shown as Fig. 1(b)].

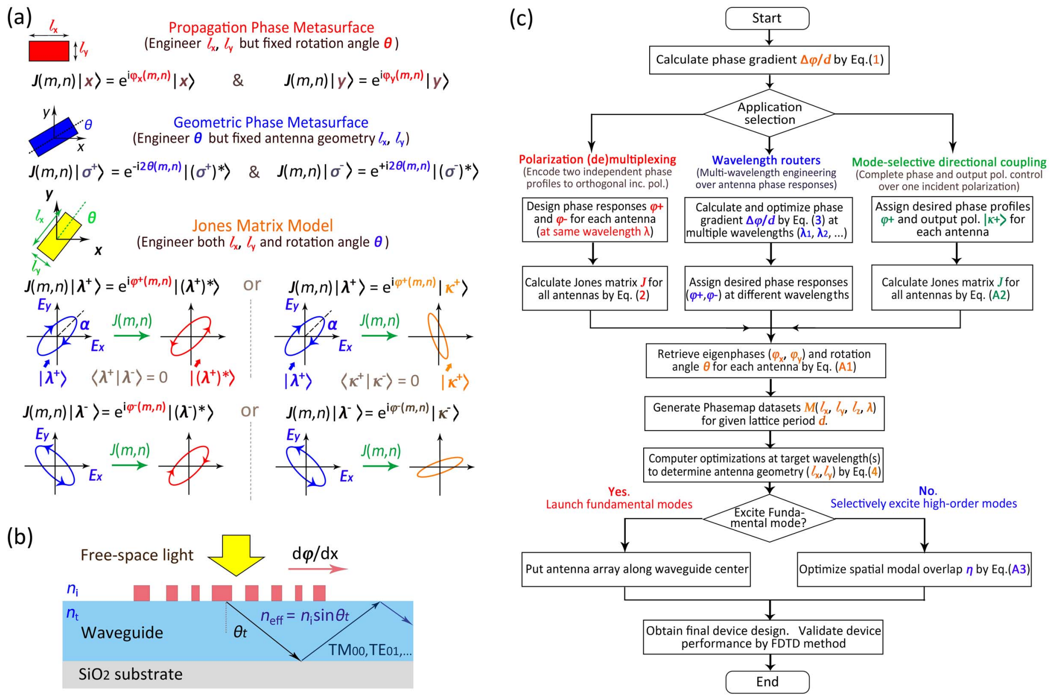

Fig. 1. (a) Metasurface concepts comparison. Propagation phase metasurface: engineered antenna geometry (l_x, l_y) but fixed rotation angle θ. Geometric phase metasurface: identical antennas with spatially varying orientation angle [39–41]. In the Jones matrix model (two working scenarios), red or orange color-highlighted phases or polarizations represent configurable parameters, while black or gray colored parts denote given or not configurable factors. (b) The normally incident light can be directionally coupled into specific waveguide modes after consecutive interactions with the gradient metasurface. (c) Flow chart for design process (detailed in Methods section).

$k_0 = 2\pi/\lambda$ stands for wave vector and λ is the vacuum light wavelength. For a gradient metasurface, we have constant phase gradient $d\Phi/dx = \Delta\varphi/d$, where $\Delta\varphi$ is the phase difference between neighboring antennas and d represents the antenna center-to-center interval or lattice period. The coupling direction is hence determined by the sign of the phase gradient.

In addition to the phase-matching condition, the spatial modal overlap η between antenna scattering near-field $\mathbf{E}_{\text{antenna}}(x, y, z)$ and the desired waveguide mode profile $\mathbf{E}_{\text{mode}}(x, y, z)$ should be optimized as well to realize mode-selective one-way coupling [17,34] [see Eq. (A3) in Appendix A]. The phase-matching condition in Eq. (1) offers instruction on the proper selection of antenna phase gradient, while Eq. (A3) manifests appropriate relative location of the array on the waveguide (elaborated in detail later).

The general design flow chart is illustrated as Fig. 1(c). Starting from different device functions, either a desired phase profile with target output polarization states or two specific phase profiles are assigned for all the antennas to realize polarization or wavelength (de)multiplexers. Computerized optimizations (see Methods for details) are then performed to calculate design parameters (such as lateral dimensions l_x, l_y and rotation angle θ) for each antenna. Numerical simulations using the full-vector finite-difference time-domain (FDTD) method are applied to verify device performance. The design method is detailed in the Methods section. In this work, we will more focus on the simplified design method under phase-matching condition (which leads to the largely enhanced coupling efficiency compared with previous research [31–33,41]) for classic polarizations and controlled excitation of high-order modes.

3. POLARIZATION DEMULTIPLEXERS FOR ARBITRARY POLARIZATIONS

Assume two arbitrary orthogonal incident polarizations $|\lambda^+\rangle$ and $|\lambda^-\rangle$. If we set the output polarization vectors as $|\kappa^+\rangle = |(\lambda^+)^*\rangle$ and $|\kappa^-\rangle = |(\lambda^-)^*\rangle$ (denoting preserved polarization ellipse but flipped chirality), we can find a Jones matrix $\mathbf{J}(m, n)$ for each $(m^{\text{th}}, n^{\text{th}})$ antenna pixel that satisfies the following two equations simultaneously: $\mathbf{J}(m,n)|\lambda^+\rangle = \exp[i\varphi^+(m,n)]|(\lambda^+)^*\rangle$ and $\mathbf{J}(m,n)|\lambda^-\rangle = \exp[i\varphi^-(m,n)]|(\lambda^-)^*\rangle$. $\varphi^+(m,n)$ and $\varphi^-(m,n)$ are two arbitrary and independent phase profiles locally imparted by antenna pixel (m, n) to incident polarizations $|\lambda^+\rangle$ and $|\lambda^-\rangle$, respectively [38–41]. The target Jones matrix $\mathbf{J}(m, n)$ can be hence solved as below:

$$\mathbf{J}(m,n) = \left[e^{i\varphi^+(m,n)}|(\lambda^+)^*\rangle, e^{i\phi^-(m,n)}|(\lambda^+)^*\rangle\right] \cdot [|\lambda^+\rangle, |\lambda^-\rangle]^{-1}. \tag{2}$$

To design polarization sorters for arbitrary incident polarizations, opposite gradient phase profiles φ^+ and φ^- are applied to $|\lambda^+\rangle$ and $|\lambda^-\rangle$, respectively, directionally coupling the orthogonal polarizations into opposite directions [48]. The required phase step $\Delta\varphi$ is then calculated from the phase-matching condition by Eq. (1) to excite the modes of interest. The desired phase profiles for each antenna $\varphi^+(m, n)$ and $\varphi^-(m, n)$ are confirmed after selecting the initial phase value φ_0 of one

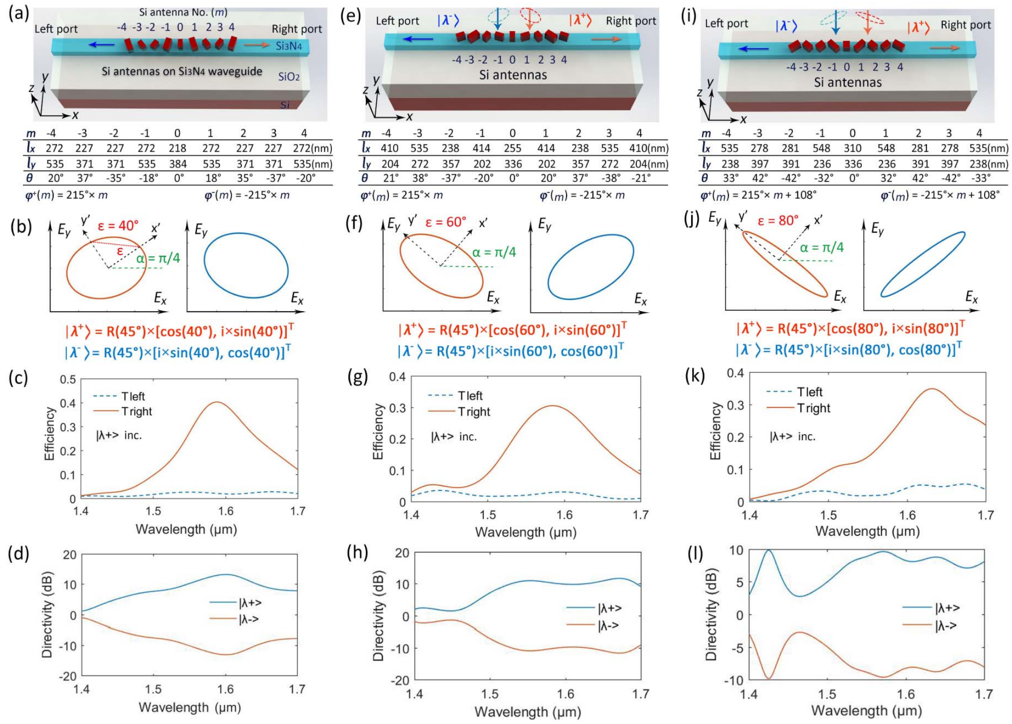

Fig. 2. Polarization (de)multiplexers for arbitrary elliptical polarizations. (a), (e), and (i) Device structure sketch for splitting arbitrary orthogonal polarizations ($|\lambda^+\rangle = R(\pi/4)\cdot[\cos(\varepsilon)|\mathbf{x}\rangle + i\times\sin(\varepsilon)|\mathbf{y}\rangle]$, $|\lambda^-\rangle = R(\pi/4)\cdot[i\times\sin(\varepsilon)|\mathbf{x}\rangle + \cos(\varepsilon)|\mathbf{y}\rangle]$) with three representative incident elliptical parameters $\varepsilon = 40°$, 60°, and 80°, respectively. Accompanied forms: antenna design details (fixed antenna height: $l_z = 1.2$ μm). (b), (f), and (j) Corresponding incident polarization illustrations. (c), (g), and (k) Coupling efficiency as a function of wavelength for $\varepsilon = 40°$, 60°, and 80°, respectively, validating that our method is applicable for arbitrary polarizations. (d), (h), and (l) Corresponding directivity spectra.

array element (φ_0 is not critical for coupling performance). For given incident polarizations $|\lambda^+\rangle$ and $|\lambda^-\rangle$, the target Jones matrices $\mathbf{J}(m,n)$ are then calculated for each antenna pixel. The design parameters (antenna geometry l_x, l_y, l_z and rotation angle θ) for all antennas can be retrieved from computer optimizations (detailed in Methods).

Figures 2(a), 2(e), and 2(i) illustrate the device structures that can directionally couple orthogonal elliptical polarizations [with three representative ellipse parameters $\varepsilon = 40°$, 60°, and 80° shown as Figs. 2(b), 2(f), and 2(j), respectively] into opposite waveguide ports. The SiN waveguide patterned with Si antennas can be fabricated by the combinations of electron-beam lithography and inductively coupled plasma-reactive ion etching (ICP-RIE) detailed in Refs. [17,49,50]. For design simplicity, the waveguide cross-sectional dimension is selected as width × height = 680 nm × 600 nm, which satisfies the single-mode transmission condition around $\lambda = 1.55$ μm, and the effective mode indices ($n_{\text{eff}} \approx 1.54$) of fundamental TE_{00} and TM_{00} modes are almost degenerate [41]. The antenna array locates at the center of the waveguide to maximize spatial modal overlap with the fundamental modes. The designed phase profiles of each antenna φ^+ and φ^- are manifested below device schematics. As is shown in Figs. 2(c), 2(g), and 2(k), polarization demultiplexing with high coupling efficiency (see Methods for definition) about 40% is achieved. We define the directivity parameter γ to quantify the directional coupling performance of the proposed device: $\gamma = 10\times\lg(T_{\text{right}}/T_{\text{left}})$, where T_{right} and T_{left} are the transmission rates of the right and left waveguide ports, respectively. In Figs. 2(d), 2(h), and 2(l), we plot the directivity curves as a function of wavelength. Excellent polarization sorting performances are achieved with maximum directivity of 13 dB, validating the applicability of the method for arbitrary polarizations.

On-chip Polarization Sorters for Classic Polarizations: Linear and circular polarizations are special cases of arbitrary elliptical polarizations, but they are important polarization states of light frequently used in experiments. Therefore, integrated polarization (de)multiplexers for classic polarizations are also briefly mentioned with high coupling efficiency but simplified design process.

For linear polarizations (for example, $|\lambda^+\rangle = |\mathbf{x}\rangle = [1,0]^T$ and $|\lambda^-\rangle = |\mathbf{y}\rangle = [0,1]^T$), we have $\varphi^+ = \varphi_x$ and $\varphi^- = \varphi_y$. Hence, the antenna geometries can be directly optimized without calculating the Jones matrix. Figure 3(a) shows the device structure that directionally couples incident $|\mathbf{x}\rangle$ polarization to the right-propagating fundamental TM_{00} mode and directs $|\mathbf{y}\rangle$ polarization into the left-propagating TE_{00} mode [as shown in Figs. 3(c)–3(e)]. Figure 3(b) shows the phase map (see Methods) used in this design. Excellent mode quality is observed at the waveguide ports [see Figs. 3(f)–3(h)]. Taking the effective mode index $n_{\text{eff}} \approx 1.55$ into Eq. (1), we have $\Delta\varphi = \pm 216°$. The designed phase profiles $\varphi^+(m)$ and $\varphi^-(m)$ for the m^{th} antenna are then assigned as $\varphi^{\pm}(m) = \pm m\cdot\Delta\varphi$. As is shown in Figs. 3(i) and 3(j), high coupling efficiency around 47% and directivity over 23 dB are achieved around $\lambda = 1.55$ μm when the phase-matching condition is satisfied.

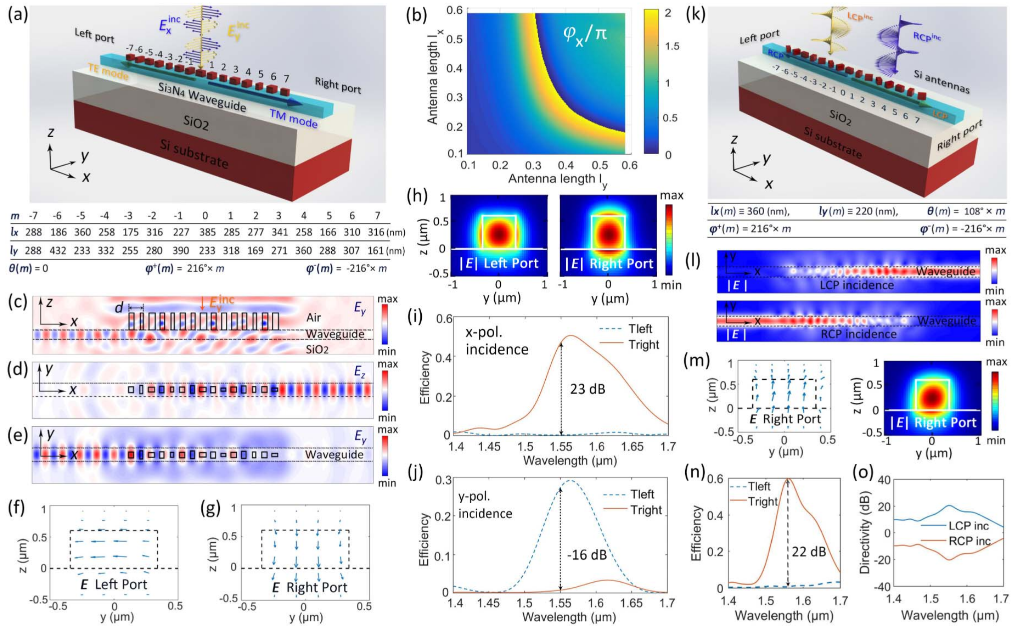

Fig. 3. (a) Device schematic of the integrated linear-polarization (de)multiplexer. Waveguide width × height = 680 nm × 600 nm. (b) Phase map showing the phase retardation of transmitted light as a function of antenna geometry (l_x, l_y) at $\lambda = 1.55$ μm with fixed antenna height $l_z = 1.2$ μm. (c) Distribution of electric field component $\mathbf{E_y}$ in the x–y plane under $|\mathbf{y}\rangle$ plane wave illumination ($\lambda = 1.55$ μm). Antenna and waveguide profiles are marked in solid and dashed lines, respectively. (d), (e) Full-wave simulations showing the directional coupling of electric field components $\mathbf{E_z}$ and $\mathbf{E_y}$ into opposite directions under illumination of linear $|\mathbf{x}\rangle$ and $|\mathbf{y}\rangle$ polarizations, respectively. (f), (g) Vector diagram of the electric field at the left (under $|\mathbf{x}\rangle$ illumination) and right ($|\mathbf{y}\rangle$ illumination) waveguide ports , respectively, at $\lambda = 1.55$ μm. (h) Corresponding electric field norm $|\mathbf{E}|$ distribution. (i), (j) Coupling efficiency spectra under $|\mathbf{x}\rangle$ and $|\mathbf{y}\rangle$ excitations, respectively. (k) Structure sketch for the circular-polarization (de)multiplexer. (l) Circular polarization demultiplexing: $|\mathbf{E}|$ distributions under incident left-handed (LCP) and right-handed circular polarization (RCP). (m) Vector diagram and $|\mathbf{E}|$ distribution at the right waveguide port (approximate TM_{00} mode) under LCP incidence ($\lambda = 1.55$ μm). (n) Coupling efficiency spectrum (LCP illumination). (o) Directivity spectrum.

For circular polarizations, our design method will give the same design results as those exploiting the geometric phase [36,41], validating the comprehensiveness of our method that accommodates both propagation and geometric phase metasurfaces. Figure 3(k) delineates the chip-integrated demultiplexer to separate circular polarizations. Excellent polarization demultiplexing functionality is numerically validated in Figs. 3(l)–3(o), with high coupling efficiency of 57% and directivity over 22 dB at $\lambda = 1.55$ μm.

4. CHIP-INTEGRATED WAVELENGTH DEMULTIPLEXERS

The Jones matrix model can also be extended to enable complete polarization and phase control over multiple wavelengths, by applying computer optimizations of phase map datasets **M** at different light wavelengths [41,51,52]. Specifically, if we deploy opposite phase gradients to signal channels with different wavelengths, chip-integrated polarization demultiplexers or compact light routers can be designed. Compared to the designs at single wavelength, multi-wavelength engineering requires more complicated optimizations [41]. Here we will give a new simplified design method that can simultaneously realize polarization and wavelength demultiplexing for classic polarizations.

As the phase is gauge independent modulo of 2π, the phase step $\Delta\varphi$ is equivalent to $\Delta\varphi' = \Delta\varphi \pm 2n\pi$, where n is an integer. Consequently, the phase-matching condition in Eq. (1) can be modified with multiple potential solutions: $n_{\mathrm{eff}} k_0 = (\Delta\varphi \pm 2n\pi)/d \cdot \mathrm{sign}(\Delta\varphi \pm 2n\pi/d)$ as long as the value of effective mode index n_{eff} still corresponds to a physical propagating mode and d remains valid subwavelength spacing. Therefore, for one given structure the phase-matching condition may be satisfied at different wavelengths λ_1 and λ_2 for two counter-propagating modes:

$$\begin{cases} \frac{\Delta\varphi_0}{d} = n_{\mathrm{eff}}|_{\lambda=\lambda_1} \cdot k_0 \\ \frac{\Delta\varphi_0 - 2\pi}{d} = -n_{\mathrm{eff}}|_{\lambda=\lambda_2} \cdot k_0 \end{cases}, \tag{3}$$

where we set $0 \le \Delta\varphi_0 < 2\pi$ as the constant phase step, and $n_{\mathrm{eff}}|_{\lambda=\lambda_1}$ and $n_{\mathrm{eff}}|_{\lambda=\lambda_2}$ are the effective indices of two waveguide modes at light wavelengths λ_1 and λ_2, respectively.

For instance, under the condition of $d = 505$ nm and $\Delta\varphi_0 = 158°$ ($\Delta\varphi_0' = \Delta\varphi_0 - 2\pi = -202°$), the unidirectional phase gradient provided by the antenna array matches the momentum difference between the incident free-space electromagnetic wave and the propagating waveguide mode. Equation (3) is hence satisfied for both right-propagating and left-propagating fundamental modes at $\lambda_1 = 1.7$ μm and $\lambda_2 = 1.45$ μm, respectively, with effective mode indices as $n_{\mathrm{eff}}|_{\lambda=\lambda_1} = 1.48$ and $n_{\mathrm{eff}}|_{\lambda=\lambda_2} = 1.61$ accordingly (waveguide width × height = 680 nm × 600 nm, antenna height $l_z = 1$ μm).

Figure 4(a) illustrates the structure that can realize wavelength and polarization demultiplexing simultaneously. As is

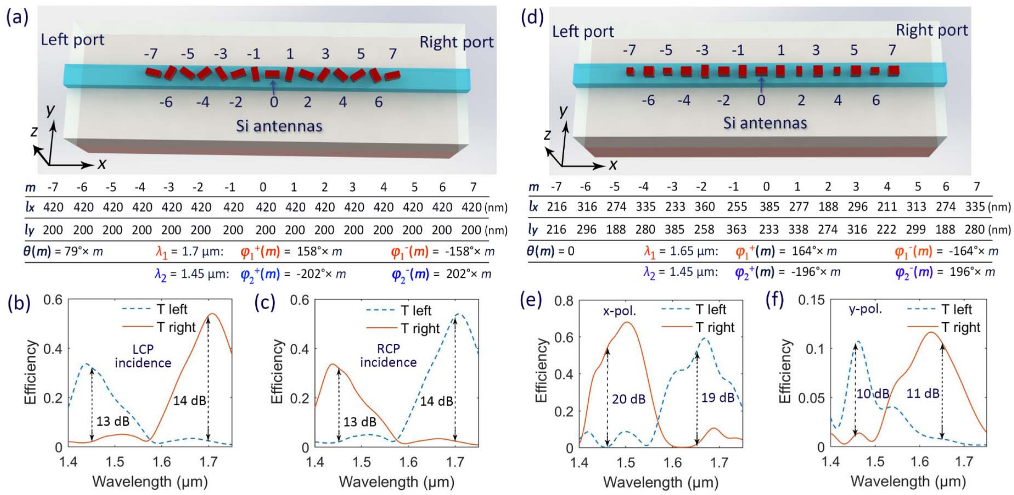

Fig. 4. (a) Structure for the multifunctional (de)multiplexer for circular polarizations. When working at a fixed wavelength, it functions as a spin/polarization demultiplexer, while under fixed incident polarizations it works as a wavelength demultiplexer/color router. (b), (c) Coupling efficiency spectrum under LCP and RCP illumination, respectively. (d)–(f) Similar to (a)–(c) but for device working for linear polarizations. The shape difference between the curves in (e) and (f) can be ascribed to the discrepancy of spatial modal overlap η under different incident polarizations.

shown in Figs. 4(b) and 4(c), at around $\lambda_1 = 1.7$ μm, incident left-handed circular polarization (LCP) or right-handed circular polarization (RCP) will be directionally coupled to the right or left port of the waveguide accordingly, with high coupling efficiency around 53% and high extinction ratio [see Fig. 4(b)] exceeding 14 dB. In contrast, at $\lambda_2 = 1.45$ μm, the incident LCP or RCP will be directed to the left or right waveguide port instead, fulling versatile integrated (de)multiplexing devices over both wavelength and polarization.

Simultaneous wavelength and polarization light routers can also be designed for linear polarizations in a similar manner; the device structure is sketched as Fig. 4(d). The phase steps are designed as $\Delta\varphi_0 = 164°$ and $\Delta\varphi_0' = -196°$ for $\lambda_1 = 1.65$ μm and $\lambda_2 = 1.45$ μm, respectively. In Figs. 4(e) and 4(f), we plot the coupling efficiency curves as a function of light wavelength for incident x- and y-polarizations, respectively. A maximum coupling efficiency over 67% (51% at operation wavelength 1.65 μm) and excellent extinction ratio of 20 dB are numerically validated.

5. MODE-SELECTIVE DIRECTIONAL COUPLERS AND ON-CHIP VORTEX BEAM GENERATOR

In previous design scenarios, single-mode waveguides are applied, where only fundamental TE_{00} and TM_{00} modes can propagate. For selective excitation of high-order modes in multimode waveguides, it is crucial to judiciously arrange the relative location of the antenna arrays to optimize the field overlap η between the near fields scattered by antenna pixels $\mathbf{E}_{\mathrm{antenna}}(x, y, z)$ and the target waveguide mode $\mathbf{E}_{\mathrm{mode}}(x, y, z)$.

We note that Eq. (A3) (in Appendix A) gives the integration of two vector fields. Therefore, the polarization state of output electric field $\mathbf{E}_{\mathrm{antenna}}(x, y, z)$ should be properly selected. By assigning the desired output polarization state $|\kappa\rangle = [\kappa_1, \kappa_2]^T$ for given incident polarization $|\lambda\rangle = [\lambda_1, \lambda_2]^T$, the target Jones matrix $\mathbf{J}(m, n)$ can be solved (see Appendix A for details) for polarization-controlled coupling. As the dominate electric field component of the TE mode is y-polarized, if we assign $|\kappa\rangle = |\mathbf{y}\rangle = [0,1]^T$, TE modes will be preferably excited such that it has much higher modal overlap than the TM mode [17,35,41]. The phase gradient $\Delta\varphi/d$ can be then judiciously selected to match the effective index of the TE mode of specific mode order. Similarly, we can apply $|\kappa\rangle = |\mathbf{x}\rangle = [1,0]^T$ to launch TM modes.

A. Integrated Directional Couplers with Mode Selectivity

For instance, Fig. 5(a) shows the device structure that couples normally incident linear y-polarization into the left-propagating TE_{00} mode and right-propagating TE_{10} mode [see Fig. 5(b)]. The waveguide dimension is selected as width × height = 1.5 μm × 0.6 μm, supporting TE_{10} and TM_{10} high-order modes. As is shown in Figs. 5(c) and 5(d), putting the antennas on the waveguide center gives good spatial modal overlap η for fundamental TE_{00} and TM_{00} modes. While for the TE_{10} mode, two rows of antennas (with interval $\Delta y \approx 0.8$ μm) can yield better η. Given the effective indices of 1.76 and 1.55 for TE_{00} and TE_{10} modes, respectively, a phase step of $\Delta\varphi = \pm 216°$ can be applied under antenna intervals $d_{\mathrm{TE}_{00}} = 0.53$ μm and $d_{\mathrm{TE}_{10}} = 0.6$ μm accordingly to meet the phase-matching condition in Eq. (1). We note that for the TE_{10} mode, a phase difference of π exists between two mode lobes [see Fig. 5(d), right panel]. Therefore, we spatially dislocate the two antenna rows by half of the mode period $\Delta x = \lambda/(2n_{\mathrm{eff}}) \approx 0.5$ μm along the x direction, making the electrical near fields between the upper and lower groups of TE_{10} antennas (with same antenna number m) be π out of phase [see the right panel of Fig. 5(c)]. The simulated output electric field norm $|\mathbf{E}_y|$ distributions are shown in Fig. 5(e), where the white dashed lines indicate the approximate location of the antenna arrays. In Fig. 5(f) we plot the corresponding output vector diagrams in the left and right waveguide ports. High mode purity (see Methods for details) of 89% and 85% is validated with respect to ideal TE_{00} and TE_{10} modes, respectively.

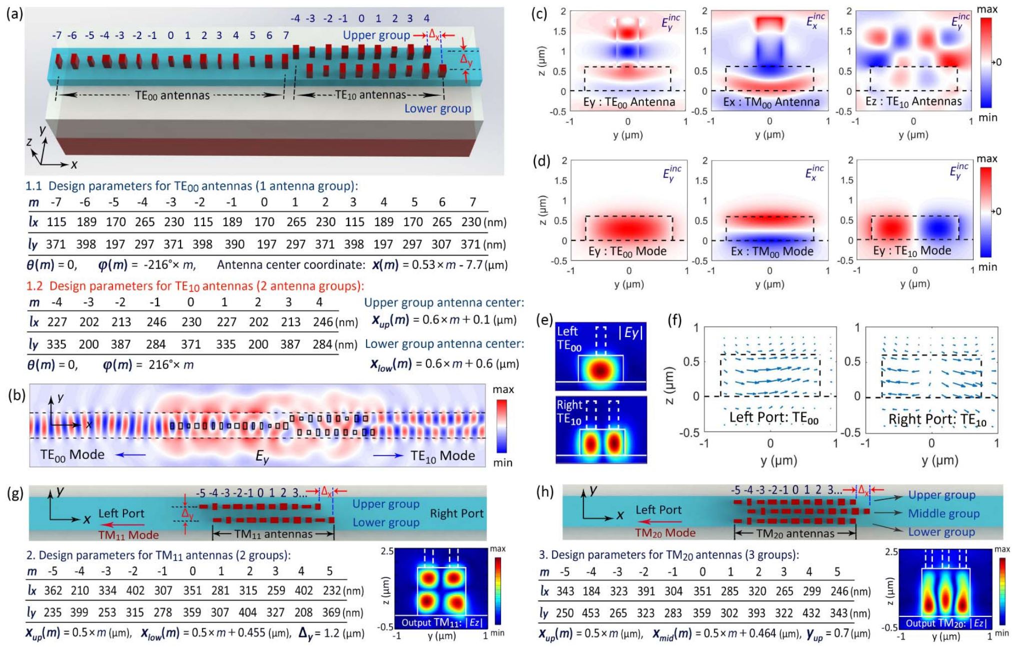

Fig. 5. (a) Device structure sketch for the waveguide-integrated mode-selective directional coupler. A left single-row antenna array (namely TE_{00} antennas) is applied to excite left-propagating TE_{00} mode. Double rows of identical antenna arrays (namely TE_{10} antennas) with dislocations of $\Delta x \approx 0.5$ μm in the x direction and $\Delta y \approx 0.8$ μm in the y direction. Accompanied form: detailed design parameters. (b) Electric field component $\mathbf{E_y}$ distribution along middle waveguide plane under the illumination of $|\mathbf{y}\rangle$ polarized plane wave. (c) Antenna near fields (see Methods). Left and middle panels: $\mathbf{E_y}$ and $\mathbf{E_x}$ distributions for an $l_x \times l_y = 0.2$ μm × 0.4 μm antenna (θ = 0°) placed at waveguide center (as TE_{00} antennas). Right panel: $\mathbf{E_z}$ distribution along the center plane between two TE_{10} antennas ($m = -4$ for upper and lower groups). (d) Electric field distributions for ideal TE_{00} ($\mathbf{E_y}$), TM_{00} ($\mathbf{E_x}$), and TE_{10} ($\mathbf{E_y}$) modes. (e) Calculated output $|\mathbf{E_y}|$ distributions for the left (upper panel) and right (lower panel) waveguide ports accordingly. (f) Corresponding vector diagram of output electric fields at waveguide ports, agreeing well with TE_{00} and TE_{10} modes. (g) Device structure (with antenna design parameters) launching left-propagating TM_{11} mode with two rows of dislocated antennas (upper and lower groups). Right panel: simulated output $|\mathbf{E_z}|$ distribution at the left waveguide port at $\lambda = 1.55$ μm. (h) Design schematic for the directional coupler to selectively excite TM_{20} mode (with three antenna rows). Antenna center coordinates: $y_{mid} = 0$, $y_{up} = -y_{low} = 0.7$ μm. Right panel: $|\mathbf{E_z}|$ distribution at the left waveguide port ($\lambda = 1.55$ μm).

To further convey the flexibility of our proposed scheme to selectively excite arbitrary waveguide modes of interest, Figs. 5(g) and 5(h) give the device structures coupling linear x-polarization into the left-propagating TM_{11} and TM_{20} modes, respectively (waveguide dimension: width × hight = 2.0 μm × 1.8 μm). The simulated output electric fields $|\mathbf{E_z}|$ are shown in the right panels with maximum coupling efficiency of 31% and high maximum mode purity approaching 70%, which is not achievable in previous reports [36,37]. In contrast, in previous similar research either solely fundamental modes are investigated [41], or only unconfigurable hybrid modes can be harvested in waveguide ports [36,37] (where one certain waveguide mode of interest cannot be exclusively excited with high mode purity). The approximate locations of the antenna groups are marked in white dashed lines, where the phase-matched gradients $\Delta\varphi$ calculated from Eq. (1) are synergized with properly engineered spatial overlap η (see Appendix A) to facilitate the controlled launching of specific high-order modes.

B. Chip-Scale Vortex Beam Generator

In the previous example in Fig. 5(a), opposite phase gradients are assigned to the TE_{00} and TE_{10} modes. If we deploy phase gradients with the same sign, the functionality of a waveguide mode mixer can be realized, which is useful in integrated mode-division multiplexing systems [15]. Furthermore, here we will also propose and demonstrate a chip-integrated vortex beam generator (simultaneously realizing OAM excitation and light coupling in a single device) to extend and validate the flexibility of our mode-control method. Featured by its helical phase front and phase singularity [53,54], optical vortices carrying OAM with various topological charge values ℓ have proven fruitful for a wide range of applications including optical communications [55–58], photonic manipulation [59], and quantum information [60].

Figures 6(a) and 6(b) illustrate a chip-integrated twisted light generator that couples a linearly y-polarized plane wave into an optical vortex carrying OAM with topological charge $\ell = +1$, which is realized by combining two high-order TE_{01} and TE_{10} modes with $\pi/2$ phase difference [61,62] [shown as Fig. 6(c)]. Similarly, we use single-row antenna array (namely TE_{01} antennas) with a phase-matched gradient ($\Delta\varphi = 216°$ and lattice period $d = 0.5$ μm) to excite the TE_{01} mode. Double-row antennas with the same phase gradient (namely TE_{10} antennas) are applied to selectively couple TE_{10} mode. Figure 6(d) illustrates the simulated output electric field norms $|\mathbf{E_y}|$ when only the TE_{01} antennas or the TE_{10} antennas exist on the waveguide (left two panels). In Figs. 6(e) and 6(f), we plot the coupling efficiency and mode purity spectra

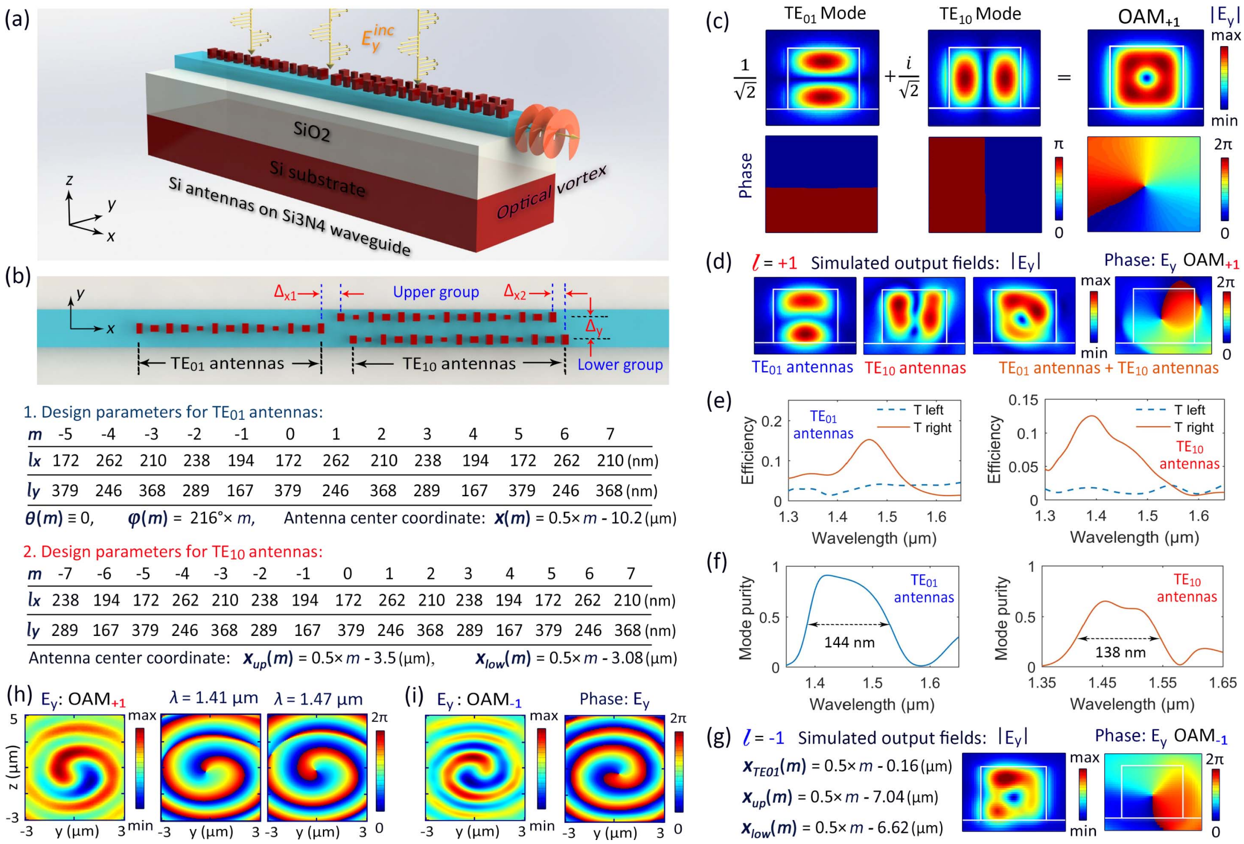

Fig. 6. (a) Device schematic for chip-integrated OAM generator: directional coupling normally incident linearly y-polarized plane wave into right-propagating optical vortex beam. (b) Top view of the device with design parameters manifested in the accompanied forms. $\Delta x_2 \approx 0.415$ μm and $\Delta y \approx 0.8$ μm. (c) Working principle illustration: combining TE_{01} and TE_{10} modes with $\pi/2$ phase difference can theoretically produce a helically phased vortex field with topological charge $\ell = +1$. Upper panels: $|\mathbf{E_y}|$ distributions for ideal TE_{01}, TE_{10} and mixed OAM modes accordingly. Lower panels: corresponding phase distributions. (d) Calculated output electric field $|\mathbf{E_y}|$ distributions when only the TE_{01} antennas exist (left panel), only TE_{10} antennas exist (middle panel), and both TE_{01} and TE_{10} antennas exist (right panels). Right most panel: corresponding (to the right panel) phase distribution at waveguide right port showing OAM_{+1} mode. White lines denote waveguide profile. (e), (f) Coupling efficiency and mode purity spectra when only the TE_{01} (left panel) or TE_{10} (right panel) antennas are present accordingly. (g) Calculated output OAM_{-1} mode [$|\mathbf{E_y}|$ and phase ($|\mathbf{E_y}|$)] distributions after re-arranging the relative locations of the TE_{01} and TE_{10} antennas in the x direction. (h), (i) Output vortex beam [instantaneous $\mathbf{E_y}$ and phase ($\mathbf{E_y}$) at $\lambda = 1.45$ μm] with $\ell = +1$ and $\ell = -1$, respectively, after exiting waveguide right port with a propagation distance of 2 μm in free space.

respectively when only the TE_{01} (left panels) or TE_{10} (right panels) antennas are present. The maximum coupling efficiency of a single array is 16% and about 9% when both of the antenna arrays are present. Meanwhile, the proposed structures exhibit broad operation bandwidth over 144 nm (full width at half-maximum of the mode purity spectrum).

As is shown in Fig. 6(b), the two antenna groups are then applied together to generate the optical vortex. The two antenna arrays have an engineered interval of $\Delta x_1 = 0.675$ μm along the x axis to realize the $\pi/2$ phase difference between the two modes, which is not exactly equal to a quarter-mode period (because the second antenna array will slightly disturb transmission of the first one). The waveguide dimension here is selected as width × height = 1.56 μm × 1.32 μm, where effective mode indices of TE_{01} and TE_{10} modes are almost degenerate ($n_{\mathrm{eff}} \approx 1.74$) to share the same phase velocity around $\lambda = 1.45$ μm. The simulated output mode profiles and corresponding phase distributions (when both TE_{01} and TE_{10} antennas are present) are shown in the last two panels of Fig. 6(d), where a doughnut-shaped intensity distribution for the optical vortex with topological charge $\ell = +1$ is observed.

By re-arranging the relative locations of the TE_{01} and TE_{10} antennas to adjust the relative phase delay [61], vortex beam generation with $\ell = -1$ can be also achieved. Figure 6(g) shows the calculated $\mathbf{E_y}$ distributions (the coordinates of each antenna center are manifested in the left panel). An azimuth (ϕ)-dependent phase profile $\exp(i\ell\phi) = \exp(-i\phi)$ featured by $\ell = -1$ OAM mode is observed. The distributions of the output vortex field $\mathbf{E_y}$ with topological charge $\ell = +1$ and -1 after exiting the waveguide are also shown in Figs. 6(h) and 6(i), respectively, indicating that high-quality vortex beams with configurable topological charge of $\ell = 1$ or -1 are successfully obtained in free space. We anticipate that our method can be readily adopted for up-scaling to generate optical vortices with higher topological charge. An integrated $\pi/2$ mode converter [63] may be also potentially helpful for launching twisted light with higher-order OAM by mode transformations [61,64]. Compared with previous methods to generate twisted light by conventional spatial light modulation [65], birefringence [66], or mode converters [62,67], our method combining light coupling and OAM conversion into a single device possesses a much smaller footprint with broad bandwidth and higher integrability.

6. DISCUSSIONS

Further discussions on the influence of illumination condition (or different types of light sources) and fabrication error on device performance are also given in this section.

A. Impact of Excitation Light Source

The absolute value of coupling efficiency highly relies on the illumination condition [27,31–33], depending on how tightly the light is focused on the antenna structures. The peripheral incident light that does not "tough" the antennas actually barely makes contribution to the coupled power into the waveguide port, thus dragging down the value of coupling efficiency [which is normalized to power of total power of the light source (see Methods)].

The total-field scattered-field (TFSF) light source [68] is commonly used to analyze antenna scattering attributes and calculate device coupling efficiency [34,36,37,69]. The coupling efficiencies of the abovementioned devices are based on the TFSF source (see Methods), which gives the most tightly focused excitation light fields around the antenna arrays. Taking the device in Fig. 4(a) as an instance, the coupling efficiencies of the same structure under different types of excitation light sources are shown in Figs. 7(a)–7(c). Diffracting plane wave illumination (truncated by a rectangular aperture) gives the lower limit of estimation for coupling efficiency about 9%. Figure 7(b) shows the results with coupling efficiency over 12% at an operation wavelength of $\lambda = 1.7$ μm, when the excitation Gaussian beam (about 8 μm above the waveguide) is focused by a thin lens with numerical aperture NA = 0.2 (see Methods for details). This experimentally easy-to-implement value can be further increased if we transform the Gaussian beam into an elliptical spot [70] and focus it on the antennas by an objective lens with a larger NA [34,69]. As is shown in the inset of Fig. 7(b), a large portion of the Gaussian beam with circular spot irradiates on the substrate, remaining futile to light coupling. If we apply a Gaussian source with an elliptical spot [see Fig. 7(c) inset], which can be easily achieved by either a deformed fiber [70] or beam transformations [61], the power of the light source is utilized in a more efficient way and the coupling efficiency is increased to about 30%.

We note that though the introduction of the phase-matching condition largely enhanced the coupling efficiency (by at least 10-fold) compared to the devices without rigorously applying it [31–33,41], increasing coupling efficiency is not considered during the computer optimizations (see Methods). Here the versatile functionalities toward polarization and wavelength (de)multiplexers or mode-selective directional couplers are more focused in the design process, instead of coupling efficiency. The coupling efficiency can be further increased by adding the efficiency parameter into the objective function in the optimization process or applying like square arrays of more antennas on a bigger waveguide.

B. Influence of Fabrication Error

The impact of fabrication error on device performance is also analyzed in Fig. 8. As is shown in Figs. 8(a) and 8(f), we assume the fabrication errors in antenna geometry (Δl_x, Δl_y, unit: nm) and rotation angle ($\Delta\theta$, unit: °) are mutually independent random variables obeying normal distribution $N(\mu, \sigma^2)$, where μ is the mathematical expectation of the distribution and σ denotes its standard deviation.

Figures 8(b)–8(d) show the coupling efficiency spectra of the device sketched in Fig. 3(a) under different extent of fabrication errors (the values of Δl_x and Δl_y for each antenna are generated by MATLAB). The device performance in Fig. 8(b) is very approaching to the designed value [the curves in Fig. 4(c) without fabrication error], when the standard deviation $\sigma = 10$ nm [with the largest fabrication error reaching $\Delta l_x(7) = 18$ nm (for antenna $m = 7$) and $\Delta l_y(-2) = -25$ nm (for antenna $m = -2$)]. In general the coupling efficiency deteriorates with larger fabrication error, as the phase-matching condition is no longer accurately satisfied. However, the device performance is still acceptable even when $\sigma = 20$ nm [see Fig. 8(c)]: the largest fabrication error reaches $\Delta l_x(-3) = 37$ nm (for antenna $m = -3$) and $\Delta l_y(-1) = 41$ nm (for antenna $m = -1$). As is shown in Fig. 8(e), excellent directional coupling performance is still preserved under all degrees of fabrication error investigated. Figures 8(g)–8(j) give the results of the coupling performance for the device in Fig. 3(k) with fabrication error in antenna rotation angle $\Delta\theta$ [illustrated in Fig. 8(f), with a fixed antenna center and values of $\Delta\theta$ generated by MATLAB for all antennas]. As is shown in Fig. 8(i), the structure is also very robust with $\sigma = 10°$ and the largest deviation of $\Delta\theta(6) = -17°$ for antenna $m = 6$.

We further validate that our designs are not very sensitive to misalignment [illustrated in Fig. 8(k)] that may occur when

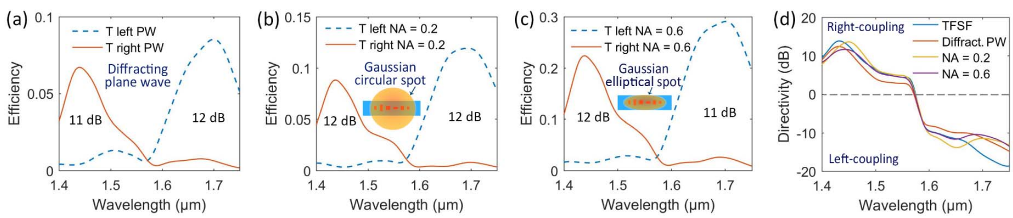

Fig. 7. Analysis on the impact of different light sources for the device in Fig. 4(a). (a)–(c) Coupling efficiency spectrum under the excitation of different (RCP) light sources: (a) diffracting plane wave (plane wave trimmed by a rectangular aperture: $x \times y = 8$ μm × 0.6 μm); (b), (c) focused Gaussian beams by a thin lens with circular (lens numerical aperture NA = 0.2) and elliptical light spot (after beam transformation with lens NA = 0.6), respectively. Insets: illumination condition sketch showing the relative size of the light spot and antenna array (see Methods). (d) Comparison of coupling directivity spectra.

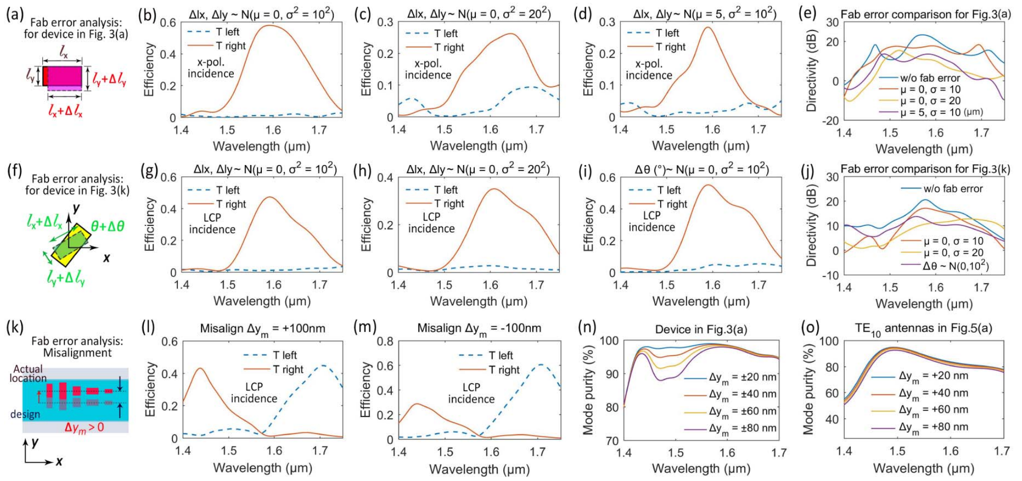

Fig. 8. (a) Illustration of fabrication (fab) error on antenna geometry. (b)–(d) Coupling efficiency spectra for device shown in Fig. 3(a) with random (independent) fabrication errors $\Delta l_x, \Delta l_y$ obeying normal distributions $\sim N(0,10^2)$, $N(0,20^2)$, and $N(5,10^2)$, respectively. (e) Comparison of directivity spectrum. (f) Sketch of an antenna cell with random fabrication error on geometry ($\Delta l_x, \Delta l_y$, unit: nm) and rotation angle ($\Delta\theta$, unit: °). (g)–(i) Coupling efficiency curves for the device in Fig. 3(k) with (g) $\Delta l_x, \Delta l_y \sim N(0,10^2)$, (h) $\Delta l_x, \Delta l_y \sim N(0,20^2)$, and (i) $\Delta\theta \sim N(0,10^2)$, respectively. (j) Directivity comparison. (k) Misalignment illustration of the whole antenna array(s) on a waveguide with positive Δy_m. (l), (m) Coupling efficiency spectra for the device in Fig. 4(a) with misalignments $\Delta y_m = +100$ nm and −100 nm, respectively. (n), (o) Comparisons of directivity spectra for the devices in Figs. 3(a) and 5(a) with different values of Δy_m.

manufacturing the antenna array(s) [17,35,49]. In Figs. 8(l) and 8(m), we plot the coupling efficiency curves under misalignment of $\Delta y_m = +100$ nm and −100 nm, respectively. Excellent (simultaneous) wavelength and polarization (de)multiplexing performances are observed for both cases, with only slightly degraded coupling efficiency under even 100 nm misalignment. Misalignment in the x direction is not considered as it poses no effect on device performance. As is shown in Figs. 8(n) and 8(o), robust mode-selective coupling attributes are still valid with high coupled-mode purity under moderate misalignment values.

7. CONCLUSIONS

A comprehensive design method targeting versatile and highly efficient on-chip light coupling and mode conversions from arbitrary incident polarizations into arbitrary waveguide modes is proposed, by synergizing the Jones matrix model with generalized Snell's law under the phase-matching condition. The coupling direction, excited mode type, and operation wavelength can be designed at will. A set of design scenarios using Si antennas-patterned SiN waveguides are numerically demonstrated around the telecommunication wavelength of 1.55 μm, including integrated polarization (de)multiplexers, wavelength routers, directional couplers with mode controllability, and chip-scale vortex beam generators.

Compared to previous research without rigorously applying the phase-matching condition [31–33,41], an at least 10-fold increment of high coupling efficiency around 67% is numerically validated. Excellent directivity around 23 dB and high extinction ratio exceeding 20 dB are also observed for the mode-selective directional couplers and wavelength (de)multiplexers, respectively. Our proposal fitting arbitrary polarizations may also outperform previous similar reports that are only applicable for circular polarizations [36,37]. Moreover, the two phase profiles locally encoded to two orthogonal elliptical polarizations can be arbitrary and independent, instead of fixed conjugated values intrinsically found in a geometric phase metasurface [37]. In addition to fundamental TE_{00} and TM_{00} modes, our systematic method can selectively and exclusively excite arbitrary high-order modes of interest [such as $TE(TM)_{01}$, $TE(TM)_{10}$, $TE(TM)_{11}$, $TE(TM)_{20}$…] with broad bandwidth and high mode purity, by engineering spatial modal overlap. To further validate our mode-control flexibility, a chip-integrated twisted light generator, coupling free-space linear polarizations into the optical vortex carrying orbital angular momentum with broad bandwidth and configurable topological charge $\ell = +1$ or −1 is also reported. Supplementary discussions also verify the robustness of our device: the high directivity and mode purity attributes are largely preserved, even under maximum random fabrication error up to 41 nm and misalignment of the antenna arrays up to ±100 nm.

We also anticipate potential extensions like ultrabroadband or enhanced manipulation over operation wavelengths by using antenna combos [71] and electrical tunable devices via applying two-dimensional materials [72–78]. Our method can be readily adopted to generate vortex beams with higher topological charges in an integrated manner. This chip-integrated metasurface platform may serve as a positive paradigm toward various optical applications, such as integrated polarization/wavelength (de)multiplexers, multifunctional mode converters, versatile waveguide couplers, configurable photonic switches, and chip-scale OAM generators for photonic integrated circuits and high-speed optical communications.

8. METHODS

A. Phase Map Generation

The phase map datasets $\mathbf{M}(l_x, l_y, l_z, \lambda) = \{\varphi_x^{\text{simulate}}, \varphi_y^{\text{simulate}}\}$ are generated by analyzing the scattering attributes of a periodic antenna array under different antenna dimensions (l_x, l_y, l_z) and light wavelengths λ using the FDTD method. In simulation, a Si antenna pixel rests on an infinitely large SiO_2 substrate, where periodic boundary conditions are applied to both $\pm x$ and $\pm y$ directions with an interval/lattice period of d to emulate array. Perfectly matched layers (PMLs) are deployed to $\pm z$ boundaries. The refractive indices are taken from measured literature values [44,79].

The antenna height l_z is properly selected to ensure a full 2π-phase coverage by altering antenna lateral dimensions (l_x, l_y). The antenna rotation angle is set as $\theta = 0°$. A linearly x-polarized plane wave is injected from the top. $\varphi_x^{\mathrm{simulate}}(l_x, l_y)$ is generated by numerically calculating the eigenphase response φ_x of the array at various combinations (l_x, l_y) by a step of 20 nm after phase compensation [80]. Cubic spline interpolations are then applied to $\varphi_x^{\mathrm{simulate}}(l_x, l_y)$. The phase map $\varphi_y^{\mathrm{simulate}}(l_x, l_y)$ under linear y-polarization can be obtained by matrix transpose $(\varphi_x^{\mathrm{simulate}})^T$ considering the symmetry of the rectangular antennas [40].

B. Antenna Geometry Selection

The target Jones matrix $\mathbf{J}(m,n)$ of each antenna pixel can be either calculated from Eq. (2) or Eq. (3), depending on the desired device functions. The required eigenphase responses $(\varphi_x^{\mathrm{design}}, \varphi_y^{\mathrm{design}})$ and antenna orientation angle θ are obtained by decomposing $\mathbf{J}(m,n)$ by Eq. (A1). Enumeration algorithms are then performed searching through $\mathbf{M}(l_x, l_y, l_z, \lambda)$ to optimize the following objective function, which will give us the optimal antenna geometry (l_x, l_y) with most approaching eigenphase responses to target values:

$$\min_{l_x, l_y}\{\max\{|\varphi_x^{\mathrm{design}} - \varphi_x^{\mathrm{simulation}}|, |\varphi_y^{\mathrm{design}} - \varphi_y^{\mathrm{simulation}}|\}\}. \tag{4}$$

C. Device Performance Validation

Device performances are numerically validated by full-vector FDTD simulations. The PML condition is applied to all boundaries. Geometric parameters of the antenna array are retrieved from the computer optimizations mentioned above. The TFSF light source [68] is applied to calculate the coupling efficiency [34,36,37,69] for all devices except Fig. 7. In Fig. 7(a), the diffracting plane wave refers to the electromagnetic fields after being truncated through a rectangular aperture (locating about 3 μm above the waveguide) with the size of 8 μm × 0.6 μm in the x and y directions. Full vectorial Gaussian beams are considered [34] in Figs. 7(b) and 7(c), as tightly focused beams are considered here for the nanoscale structures. The spot diameter in Fig. 7(b) is around 6 μm, while the transformed elliptical Gaussian beam [70] has a major axis around 6 μm and a minor axis about 0.8 μm. The coupling efficiency is defined as the ratio of the power transmitted through one certain waveguide port P_{out} and the power of the total light source [34–36], where P_{out} is calculated by integrating the Poynting vector along the monitored plane (bigger than the waveguide cross section to accommodate evanescent field). The monitored waveguide ports are more than 10 μm away from the antennas.

The antenna near fields in Fig. 5(c) are obtained by subtracting two electric fields calculated from pairs of simulations: one with antennas located at the waveguide top surface and the other with only bare waveguide [17,35]. Mode purity is defined as the ratio of the target waveguide mode power P_{mode} and total output power P_{out} [17], where P_{mode} is retrieved from the eigenmode expansion method [12,17].

APPENDIX A

Supplementary equations and brief explanations are appended. The reciprocal nature of the system [81] and pure phase modulation assumption [40,41,43] guarantee $\mathbf{J}$ to be a unitary and symmetric matrix, thus decomposable in terms of its eigenvalues and eigenvectors:

$$\mathbf{J} = \begin{bmatrix} j_{xx} & j_{xy} \\ j_{xy} & j_{yy} \end{bmatrix} = \mathbf{R}(-\theta)\begin{bmatrix} e^{i\varphi_x} & 0 \\ 0 & e^{i\varphi_y} \end{bmatrix}\mathbf{R}(\theta), \tag{A1}$$

where $\mathbf{R}(\theta) = \left[\begin{smallmatrix} \cos\theta & -\sin\theta \\ \sin\theta & \cos\theta \end{smallmatrix}\right]$ is a real unitary matrix denoting rotation transformation by an angle θ and φ_x and φ_y can then be comprehended as eigenphases when the incident electric field vector is linearly polarized along the antenna's two symmetric axes.

Consider the mapping between two arbitrary incident $|\lambda\rangle = [\lambda_1, \lambda_2]^T$ and transmitted polarizations $|\kappa\rangle = [\kappa_1, \kappa_2]^T$ interfaced by an antenna with Jones matrix $\mathbf{J}(m,n)$: $\mathbf{J}(m,n)|\lambda\rangle = |\kappa\rangle$. The matrix elements of $\mathbf{J}(m,n)$ can be solved by combining this equation with the symmetric and unitary constraints of $\mathbf{J}(m,n)$ [40,41]:

$$[j_{xx}, j_{xy}]^T = [[|\kappa^*\rangle, |\lambda\rangle]^T]^{-1} \cdot [\lambda_1^*, \kappa_1]^T \quad \text{and}$$
$$j_{yy} = -j_{xx}^* \cdot \exp(2i\angle j_{xy}), \tag{A2}$$

where $\angle j_{xy} = \arctan[\mathrm{Im}(j_{xy})/\mathrm{Re}(j_{xy})]$ represents the argument of j_{xy}. Superscripts -1 and $*$ denote the matrix inversion and complex conjugate, respectively. Mode-selective coupling is then achieved by simultaneously engineering and synergizing output polarization state $|\kappa\rangle$ and spatial modal overlap η.

The spatial overlap η of antenna near fields $\mathbf{E}_{\mathrm{antenna}}$ and one certain waveguide mode profile $\mathbf{E}_{\mathrm{mode}}(x,y,z)$ can be quantified by the following equation, where the waveguide is extended along the x direction:

$$\eta \propto \frac{|\iint \mathbf{E}_{\mathrm{antenna}}(x,y,z) \cdot \mathbf{E}_{\mathrm{mode}}^*(x,y,z)\mathrm{d}y\mathrm{d}z|^2}{(\iint |\mathbf{E}_{\mathrm{antenna}}(x,y,z)|^2\mathrm{d}y\mathrm{d}z) \cdot (\iint |\mathbf{E}_{\mathrm{mode}}(x,y,z)|^2\mathrm{d}y\mathrm{d}z)}. \tag{A3}$$

The number of total antenna arrays equals the number of the lobes (of a waveguide mode) in the transverse (y) direction (i.e., to excite the $TE_{M,N}$ mode, M arrays of antennas are needed). The mode order N is then addressed by properly selecting the matched phase gradient discussed in Eq. (1). The antenna arrays are arranged in the y direction [coordinates are shown in Fig. 5(a)], each array corresponding to the location of a waveguide mode lobe with maximum intensity [illustrated as the white dashed lines in Figs. 5(e), 5(g), and 5(h)]. The antenna arrays are dislocated along the x direction to match the relative phase difference (π) between different lobes. In general incident $|\mathbf{y}\rangle$ and $|\mathbf{x}\rangle$ polarizations are used to excite TE and TM modes, respectively. The SiN waveguide is selected also as it would be easier toward waveguide-mode management, and under the same waveguide dimension, the SiN waveguide supports fewer modes compared with the Si waveguide.

Funding. National Natural Science Foundation of China (61675114, 61875103, 61935013, 61975133, U1701661); Natural Science Foundation of Beijing Municipality (501100004826); Tsinghua University Initiative Scientific Research Program (20151080709); Beijing Young Talents Support Project (2017000020124G044).

Acknowledgment. The authors would like to thank Prof. Yuanmu Yang and Benfeng Bai from Tsinghua University for assistance with simulations and Prof. Jeehwan Kim from Massachusetts Institute of Technology and Dr. Yijie Shen from University of Southampton for helpful discussions.

Disclosures. The authors declare no conflicts of interest.

†These authors contributed equally to this work.

REFERENCES

1. D. Marpaung, J. Yao, and J. Capmany, "Integrated microwave photonics," Nat. Photonics **13**, 80–90 (2019).
2. Y. Shen, N. C. Harris, S. Skirlo, M. Prabhu, T. Baehr-Jones, M. Hochberg, X. Sun, S. Zhao, H. Larochelle, D. Englund, and M. Soljacic, "Deep learning with coherent nanophotonic circuits," Nat. Photonics **11**, 441–446 (2017).
3. M. Chamanzar, Z. Xia, S. Yegnanarayanan, and A. Adibi, "Hybrid integrated plasmonic-photonic waveguides for on-chip localized surface plasmon resonance (LSPR) sensing and spectroscopy," Opt. Express **21**, 32086–32098 (2013).
4. P. T. Lin, V. Singh, H.-Y. G. Lin, T. Tiwald, L. C. Kimerling, and A. M. Agarwal, "Low-stress silicon nitride platform for mid-infrared broadband and monolithically integrated microphotonics," Adv. Opt. Mater. **1**, 732–739 (2013).
5. M. Kues, C. Reimer, P. Roztocki, L. R. Cortes, S. Sciara, B. Wetzel, Y. Zhang, A. Cino, S. T. Chu, B. E. Little, D. J. Moss, L. Caspani, J. Azana, and R. Morandotti, "On-chip generation of high-dimensional entangled quantum states and their coherent control," Nature **546**, 622–626 (2017).
6. J. Wang, S. Paesani, Y. Ding, R. Santagati, P. Skrzypczyk, A. Salavrakos, J. Tura, R. Augusiak, L. Mancinska, D. Bacco, D. Bonneau, J. W. Silverstone, Q. Gong, A. Acin, K. Rottwitt, L. K. Oxenlowe, J. L. O'Brien, A. Laing, and M. G. Thompson, "Multidimensional quantum entanglement with large-scale integrated optics," Science **360**, 285–291 (2018).
7. D. A. B. Miller, "Optical interconnects to silicon," IEEE J. Sel. Top. Quantum Electron. **6**, 1312–1317 (2000).
8. X. Qiu, X. Ruan, Y. Li, and F. Zhang, "Multi-layer MOS capacitor based polarization insensitive electro-optic intensity modulator," Opt. Express **26**, 13902–13914 (2018).
9. L. Zhu, W. Yang, and C. Chang-Hasnain, "Very high efficiency optical coupler for silicon nanophotonic waveguide and single mode optical fiber," Opt. Express **25**, 18462–18473 (2017).
10. S. Molesky, Z. Lin, A. Y. Piggott, W. Jin, J. Vuckovic, and A. W. Rodriguez, "Inverse design in nanophotonics," Nat. Photonics **12**, 659–670 (2018).
11. A. Mohanty, M. Zhang, A. Dutt, S. Ramelow, P. Nussenzveig, and M. Lipson, "Quantum interference between transverse spatial waveguide modes," Nat. Commun. **8**, 14010 (2017).
12. R. Hunsperger, *Integrated Optics: Theory and Technology* (Springer, 1991).
13. X. Chen, C. Li, C. K. Y. Fung, S. M. G. Lo, and H. K. Tsang, "Apodized waveguide grating couplers for efficient coupling to optical fibers," IEEE Photonics Technol. Lett. **22**, 1156–1158 (2010).
14. J. Wang, S. He, and D. Dai, "On-chip silicon 8-channel hybrid (de)multiplexer enabling simultaneous mode- and polarization-division-multiplexing," Laser Photonics Rev. **8**, L18–L22 (2014).
15. L.-W. Luo, N. Ophir, C. P. Chen, L. H. Gabrielli, C. B. Poitras, K. Bergmen, and M. Lipson, "WDM-compatible mode-division multiplexing on a silicon chip," Nat. Commun. **5**, 3069 (2014).
16. M. Khorasaninejad and F. Capasso, "Metalenses: versatile multifunctional photonic components," Science **358**, eaam8100 (2017).
17. Z. Li, M.-H. Kim, C. Wang, Z. Han, S. Shrestha, A. C. Overvig, M. Lu, A. Stein, A. M. Agarwal, M. Loncar, and N. Yu, "Controlling propagation and coupling of waveguide modes using phase-gradient metasurfaces," Nat. Nanotechnol. **12**, 675–683 (2017).
18. N. Yu and F. Capasso, "Flat optics with designer metasurfaces," Nat. Mater. **13**, 139–150 (2014).
19. G. Zheng, H. Muhlenbernd, M. Kenney, G. Li, T. Zentgraf, and S. Zhang, "Metasurface holograms reaching 80% efficiency," Nat. Nanotechnol. **10**, 308–312 (2015).
20. X. Ni, Z. J. Wong, M. Mrejen, Y. Wang, and X. Zhang, "An ultrathin invisibility skin cloak for visible light," Science **349**, 1310–1314 (2015).
21. X. Zhu, W. Yan, U. Levy, N. A. Mortensen, and A. Kristensen, "Resonant laser printing of structural colors on high-index dielectric metasurfaces," Sci. Adv. **3**, e1602487 (2017).
22. Y. Hu, X. Luo, Y. Chen, Q. Liu, X. Li, Y. Wang, N. Liu, and H. Duan, "3D-integrated metasurfaces for full-colour holography," Light: Sci. Appl. **8**, 86 (2019).
23. X. Duan, S. Kamin, and N. Liu, "Dynamic plasmonic colour display," Nat. Commun. **8**, 14606 (2017).
24. A. E. Minovich, A. E. Miroshnichenko, A. Y. Bykov, T. V. Murzina, D. N. Neshev, and Y. S. Kivshar, "Functional and nonlinear optical metasurfaces," Laser Photonics Rev. **9**, 195–213 (2015).
25. Y. Yang, W. Wang, P. Moitra, I. I. Kravchenko, D. P. Briggs, and J. Valentine, "Dielectric meta-reflectarray for broadband linear polarization conversion and optical vortex generation," Nano Lett. **14**, 1394–1399 (2014).
26. B. Yang, Q. Guo, B. Tremain, R. Liu, L. E. Barr, Q. Yan, W. Gao, H. Liu, Y. Xiang, J. Chen, C. Fang, A. Hibbins, L. Lu, and S. Zhang, "Ideal Weyl points and helicoid surface states in artificial photonic crystal structures," Science **359**, 1013–1016 (2018).
27. L. Novotny and N. van Hulst, "Antennas for light," Nat. Photonics **5**, 83–90 (2011).
28. S. Sun, Q. He, S. Xiao, Q. Xu, X. Li, and L. Zhou, "Gradient-index meta-surfaces as a bridge linking propagating waves and surface waves," Nat. Mater. **11**, 426–431 (2012).
29. L. Huang, X. Chen, B. Bai, Q. Tan, G. Jin, T. Zentgraf, and S. Zhang, "Helicity dependent directional surface plasmon polariton excitation using a metasurface with interfacial phase discontinuity," Light: Sci. Appl. **2**, e70 (2013).
30. F. B. Arango, A. Kwadrin, and A. F. Koenderink, "Plasmonic antennas hybridized with dielectric waveguides," ACS Nano **6**, 10156–10167 (2012).
31. R. Guo, M. Deckera, I. Staude, D. N. Neshev, and Y. S. Kivshar, "Bidirectional waveguide coupling with plasmonic Fano nanoantennas," Appl. Phys. Lett. **105**, 053114 (2014).
32. R. Guo, M. Decker, F. Setzpfandt, I. Staude, D. N. Neshev, and Y. S. Kivshar, "Plasmonic Fano nanoantennas for on-chip separation of wavelength-encoded optical signals," Nano Lett. **15**, 3324–3328 (2015).
33. R. Guo, M. Decker, F. Setzpfandt, X. Gai, D.-Y. Choi, R. Kiselev, A. Chipouline, I. Staude, T. Pertsch, D. N. Neshev, and Y. S. Kivshar, "High-bit rate ultra-compact light routing with mode-selective on-chip nanoantennas," Sci. Adv. **3**, e1700007 (2017).
34. Y. Meng, F. Hu, Y. Shen, Y. Yang, Q. Xiao, X. Fu, and M. Gong, "Ultracompact graphene-assisted tunable waveguide couplers with high directivity and mode selectivity," Sci. Rep. **8**, 13362 (2018).
35. R. Wang, Q. Wu, W. Cai, Q. Zhang, H. Xiong, B. Zhang, J. Qi, J. Yao, and J. Xu, "Broadband on-chip terahertz asymmetric waveguiding via phase-gradient metasurface," ACS Photonics **6**, 1774–1779 (2019).
36. Y. Guo, M. Pu, X. Li, X. Ma, S. Song, Z. Zhao, and X. Luo, "Chip-integrated geometric metasurface as a novel platform for directional coupling and polarization sorting by spin-orbit interaction," IEEE J. Sel. Top. Quantum Electron. **24**, 4700107 (2018).
37. Y. Zhang, Z. Li, W. Liu, Z. Li, H. Cheng, S. Chen, and J. Tian, "Spin-selective and wavelength-selective demultiplexing based on

waveguide-integrated all-dielectric metasurfaces," Adv. Opt. Mater. **7**, 1801273 (2019).
38. R. C. Devlin, A. Ambrosio, N. A. Rubin, J. P. B. Mueller, and F. Capasso, "Arbitrary spin-to-orbital angular momentum conversion of light," Science **358**, 896–901 (2017).
39. J. P. B. Mueller, N. A. Rubin, R. C. Devlin, B. Groever, and F. Capasso, "Metasurface polarization optics: independent phase control of arbitrary orthogonal states of polarization," Phys. Rev. Lett. **118**, 113901 (2017).
40. A. Arbabi, Y. Horie, M. Bagheri, and A. Faraon, "Dielectric metasurfaces for complete control of phase and polarization with subwavelength spatial resolution and high transmission," Nat. Nanotechnol. **10**, 937–943 (2015).
41. Y. Meng, F. Hu, Z. Liu, P. Xie, Y. Shen, Q. Xiao, X. Fu, S.-H. Bae, and M. Gong, "Chip-integrated metasurface for versatile and multi-wavelength control of light couplings with independent phase and arbitrary polarization," Opt. Express **27**, 16425–16439 (2019).
42. M. Berry, "The adiabatic phase and Pancharatnam's phase for polarized light," J. Mod. Opt. **34**, 1401–1407 (1987).
43. M. Khorasaninejad and K. B. Crozier, "Silicon nanofin grating as a miniature chirality-distinguishing beam-splitter," Nat. Commun. **5**, 5386 (2014).
44. D. J. Moss, R. Morandotti, A. L. Gaeta, and M. Lipson, "New CMOS-compatible platforms based on silicon nitride and Hydex for nonlinear optics," Nat. Photonics **7**, 597–607 (2013).
45. H.-X. Xu, G. Hu, Y. Li, L. Han, J. Zhao, Y. Sun, F. Yuan, G.-M. Wang, Z. H. Jiang, X. Ling, T. J. Cui, and C.-W. Qiu, "Interference-assisted kaleidoscopic meta-plexer for arbitrary spin-wavefront manipulation," Light: Sci. Appl. **8**, 3 (2019).
46. H.-X. Xu, G. Hu, L. Han, M. Jiang, Y. Huang, Y. Li, X. Yang, X. Ling, L. Chen, J. Zhao, and C.-W. Qiu, "Chirality-assisted high-efficiency metasurfaces with independent control of phase, amplitude, and polarization," Adv. Opt. Mater. **7**, 1801479 (2019).
47. M. Khorasaninejad, W. T. Chen, R. C. Devlin, J. Oh, A. Y. Zhu, and F. Capasso, "Metalenses at visible wavelengths: diffraction-limited focusing and subwavelength resolution imaging," Science **352**, 1190–1194 (2016).
48. N. Yu, P. Genevet, M. A. Kats, F. Aieta, J.-P. Tetienne, F. Capasso, and Z. Gaburro, "Light propagation with phase discontinuities: generalized laws of reflection and refraction," Science **334**, 333–337 (2011).
49. C. Wang, Z. Li, M.-H. Kim, X. Xiong, X.-F. Ren, G.-C. Guo, N. Yu, and M. Loncar, "Metasurface-assisted phase-matching-free second harmonic generation in lithium niobate waveguides," Nat. Commun. **8**, 2098 (2017).
50. B. Wu, A. Kumar, and S. Pamarthy, "High aspect ratio silicon etch: a review," J. Appl. Phys. **108**, 051101 (2010).
51. H. Kwon, E. Arbabi, S. M. Kamali, M. Faraji-Dana, and A. Faraon, "Single-shot quantitative phase gradient microscopy using a system of multifunctional metasurfaces," Nat. Photonics **13**, 109–114 (2019).
52. T. Shegai, S. Chen, V. D. Miljkovic, G. Zengin, P. Johansson, and M. Kall, "A bimetallic nanoantenna for directional colour routing," Nat. Commun. **2**, 481 (2011).
53. Y. Shen, X. Wang, Z. Xie, C. Min, X. Fu, Q. Liu, M. Gong, and X. Yuan, "Optical vortices 30 years on: OAM manipulation from topological charge to multiple singularities," Light: Sci. Appl. **8**, 90 (2019).
54. W.-Y. Tsai, Q. Sun, G. Hu, P. C. Wu, R. J. Lin, C.-W. Qiu, K. Ueno, H. Misawa, and D. P. Tsai, "Twisted surface plasmons with spin-controlled gold surfaces," Adv. Opt. Mater. **7**, 1801060 (2019).
55. J. Wang, "Advances in communications using optical vortices," Photon. Res. **4**, B14–B28 (2016).
56. T. Lei, M. Zhang, Y. Li, P. Jia, G. N. Liu, X. Xu, Z. Li, C. Min, J. Lin, C. Yu, H. Niu, and X. Yuan, "Massive individual orbital angular momentum channels for multiplexing enabled by Dammann gratings," Light: Sci. Appl. **4**, e257 (2015).
57. Z. Xie, T. Lei, F. Li, H. Qiu, Z. Zhang, H. Wang, C. Min, L. Du, Z. Li, and X. Yuan, "Ultra-broadband on-chip twisted light emitter for optical communications," Light: Sci. Appl. **7**, 18001 (2018).
58. Z. Xie, S. Gao, T. Lei, S. Feng, Y. Zhang, F. Li, J. Zhang, Z. Li, and X. Yuan, "Integrated (de)multiplexer for orbital angular momentum fiber communication," Photon. Res. **6**, 743–749 (2018).
59. D. G. Grier, "A revolution in optical manipulation," Nature **424**, 810–816 (2003).
60. Z.-Q. Zhou, Y.-L. Hua, X. Liu, G. Chen, J.-S. Xu, Y.-J. Han, C.-F. Li, and G.-C. Guo, "Quantum storage of three-dimensional orbital-angular-momentum entanglement in a crystal," Phys. Rev. Lett. **115**, 070502 (2015).
61. A. M. Yao and M. J. Padgett, "Orbital angular momentum: origins, behavior and applications," Adv. Opt. Photonics **3**, 161–204 (2011).
62. D. Zhang, X. Feng, K. Cui, F. Liu, and Y. Huang, "Generating in-plane optical orbital angular momentum beams with silicon waveguides," IEEE Photonics J. **5**, 2201206 (2013).
63. J. Jia, Q. Li, K. Zhang, D. Chen, C. Wang, H. Gao, F. Li, and P. Zhang, "Integrated design of converter and its experimental performance," Appl. Opt. **57**, 6076–6082 (2018).
64. Y. Shen, Y. Meng, X. Fu, and M. Gong, "Wavelength-tunable Hermite-Gaussian modes and an orbital-angular-momentum-tunable vortex beam in a dual-off-axis pumped Yb:CALGO laser," Opt. Lett. **43**, 291–294 (2018).
65. L. Chen, J. Lei, and J. Romero, "Quantum digital spiral imaging," Light: Sci. Appl. **3**, e153 (2014).
66. S. Zheng and J. Wang, "On-chip orbital angular momentum modes generator and (de)multiplexer based on trench silicon waveguides," Opt. Express **25**, 18492–18501 (2017).
67. X. Zhang, A. Wang, R. Chen, Y. Zhou, H. Ming, and Q. Zhan, "Generation and conversion of higher order optical vortices in optical fiber with helical fiber Bragg gratings," J. Lightwave Technol. **34**, 2413–2418 (2016).
68. J. Schneider and K. Abdijalilov, "Analytic field propagation TFSF boundary for FDTD problems involving planar interfaces: PECs, TE, and TM," IEEE Trans. Antennas Propag. **54**, 2531–2542 (2006).
69. D. Vercruysse, P. Neutens, L. Lagae, N. Verellen, and P. V. Dorpe, "Single asymmetric plasmonic antenna as a directional coupler to a dielectric waveguide," ACS Photonics **4**, 1398–1402 (2017).
70. X. Liang, Y. Li, Z. Geng, and Z. Liu, "Selective transverse mode operation of a fiber laser based on few-mode FBG for rotation sensing," Opt. Express **27**, 37964–37974 (2019).
71. W. T. Chen, A. Y. Zhu, V. Sanjeev, M. Khorasaninejad, Z. Shi, E. Lee, and F. Capasso, "A broadband achromatic metalens for focusing and imaging in the visible," Nat. Nanotechnol. **13**, 220–226 (2018).
72. J. Kim, H. Son, D. J. Cho, B. Geng, W. Regan, S. Shi, K. Kim, A. Zettl, Y.-R. Shen, and F. Wang, "Electrical control of optical plasmon resonance with graphene," Nano Lett. **12**, 5598–5602 (2012).
73. Y. Meng, S. Ye, Y. Shen, Q. Xiao, X. Fu, R. Lu, Y. Liu, and M. Gong, "Waveguide engineering of graphene optoelectronics–modulators and polarizers," IEEE Photonics J. **10**, 6600217 (2018).
74. W. Kong, H. Kum, S.-H. Bae, J. Shim, H. Kim, L. Kong, Y. Meng, K. Wang, C. Kim, and J. Kim, "Path towards graphene commercialization from lab to market," Nat. Nanotechnol. **14**, 927–938 (2019).
75. C. Choi, J. Huang, H.-C. Cheng, H. Kim, A. K. Vinod, S.-H. Bae, V. O. Ozcelik, R. Grassi, J. Chae, S.-W. Huang, X. Duan, K. Kaasbjerg, T. Low, and C. W. Wong, "Enhanced interlayer neutral excitons and trions in trilayer van der Waals heterostructures," npj 2D Mater. Appl. **2**, 30 (2018).
76. S.-H. Bae, H. Kum, W. Kong, Y. Kim, C. Choi, B. Lee, P. Lin, Y. Park, and J. Kim, "Integration of bulk materials with two-dimensional materials for physical coupling and applications," Nat. Mater. **18**, 550–560 (2019).
77. F. Peyskens, C. Chakraborty, M. Muneeb, D. V. Thourhout, and D. Englund, "Integration of single photon emitters in 2D layered materials with a silicon nitride photonic chip," Nat. Commun. **10**, 4435 (2019).
78. G. Hu, X. Hong, K. Wang, J. Wu, H. Xu, W. Zhao, W. Liu, S. Zhang, F. Garcia-Vidal, B. Wang, P. Lu, and C.-W. Qiu, "Coherent steering of nonlinear chiral valley photons with a synthetic metasurface," Nat. Photonics **13**, 467–472 (2019).
79. E. D. Palik, *Handbook of Optical Constants of Solids II* (Boston Academic, 1998).
80. B. C. Wadell, *Transmission Line Design Handbook* (Artech House, 1991).
81. D. L. Sounas and A. Alu, "Non-reciprocal photonics based on time modulation," Nat. Photonics **11**, 774–783 (2017).